# Design and Experimental Equilibrium Stability Assessment of a RFRFR Continuum Parallel Robot

Federico Zaccaria, Edoardo Idá, Sébastien Briot

# Design and Experimental Equilibrium Stability Assessment of a RFRFR Continuum Parallel Robot

Federico Zaccaria[a,b,*], Edoardo Idà[a], Sébastien Briot[c]

[a]*Department of Industrial Engineering, University of Bologna, 28, Via Terracini , Bologna, 40126, , Italy*
[b]*Laboratoire des Sciences du Numérique de Nantes, Ecole Centrale de Nantes (LS2N), 1, Rue de la Noë, Nantes, 44300, France,*
[c]*Laboratoire des Sciences du Numérique (LS2N), Centre National de la Recherche Scientifique (CNRS), 1, Rue de la Noë, Nantes, 44300, France,*

**Abstract**

Continuum parallel robots (*CPRs*) are mainly constituted by flexible links arranged in parallel between a rigid platform and a rigid base, and they promise remarkable performance in human-robot collaboration applications. New *CPRs* modelling strategies and their experimental validation are continuously investigated due to the nonlinear phenomena complexity and the high computational effort required to solve them. This work focuses on the experimental validation of *CPRs* equilibrium stability prediction. We demonstrate that models based on planar displacement assumptions may fail in the equilibrium stability prediction, even though the *CPR* is nominally planar. A new *CPR* prototype for planar applications is proposed, designed, and tested for the scope. Unstable configurations that limit the robot workspace are theoretically and experimentally investigated. A singularity type, related to out-of-the-plane uncontrolled motions of the planar *CPR*, is experimentally identified for the first time. Experiments demonstrate that, even though the prototype is theoretically planar, a planar model neglecting out-of-the-plane phenomena is inadequate to assess equilibrium stability limits.

*Keywords:*
Continuum Parallel Robots, Model Validation, Equilibrium Stability, Singularities

## 1. Introduction

Continuum robots (*CRs*) are usually constituted by flexible components and designed to achieve safe human-robot interactions in a shared environment. Commonly, *CRs* resemble serial manipulators and may suffer from reduced payload capability, which limits their applicability. Nevertheless, *CRs* are usually well suited for small-scale surgical tasks where their intrinsic compliance grants various advantages [1]. Continuum parallel robots (*CPRs*) [2] were later introduced for achieving a good trade-off between the higher payload capability typical of rigid links parallel manipulators and the intrinsic safety of continuum robots. *CPRs* promise interesting features for large-scale or collaborative industrial tasks where the inherent flexibility of *CPRs* may be used as a safety feature. The basic concept of a continuum parallel robot was introduced in [2], where several flexible beams placed in a Gough-Stewart-like parallel arrangement were translated at their base to move a rigid platform. Although similar robot architectures were later proposed [3], [4], [5], there is a growing number of different *CPR* designed explicitly for the task they are intended for [6], [7], [8]. Relevant examples of *CPRs* applications include pick-and-place [9] or micrometre positioning [10].

*CRs* modelling received significant attention from the research community, and the literature is vast [11]. Alternative models provide a different trade-off between accuracy and computational complexity, and choosing the appropriate model for the problem at hand is an open question. To this end, experimental data and simulations of different models have been compared in many works [12], [13], [14]. Pose accuracy, namely, the model ability to correctly predict the position and orientation of the robot's end-effector (*EE*), received significant attention: lumped parameter approximations [15], [16], piecewise constant strains models [17], and shooting approaches [18], [19], are some of the most relevant examples of experimentally verified *CRs* models. For *CPRs*, the pose accuracy of the shooting method was investigated in [9] and [10] on a 2, and 3-*DoF* planar *CPRs*, respectively, and in [20] on a 6-*DoF CPR*; additionally, [21] focused on model parameter calibration. The constant curvature approach, which is suitable for tendon-driven links, was also tested in [22] and, finally, discretization through small segments was experimentally validated for spatial *CPRs* in [23].

Although pose accuracy is a significant issue for control, other robot properties are relevant for characterization and performance evaluation. Due to the high elasticity and possibly limited payload capability of *CRs*, robot stiffness and workspace (*WS*) extension are widely investigated. A *CPRs* stiffness prediction obtained by a discretization approach was experimentally validated in [24], and the *WS* of a 6-*DoF* prototype experimentally verified in [25] by comparing theoretical and actual posed on several *WS* slices. Recently, the phenomena limiting

*Corresponding author
*Email addresses:* federico.zaccaria3@unibo.it (Federico Zaccaria), edoardo.ida2@unibo.it (Edoardo Idà), sebastien.briot@ls2n.fr (Sébastien Briot)

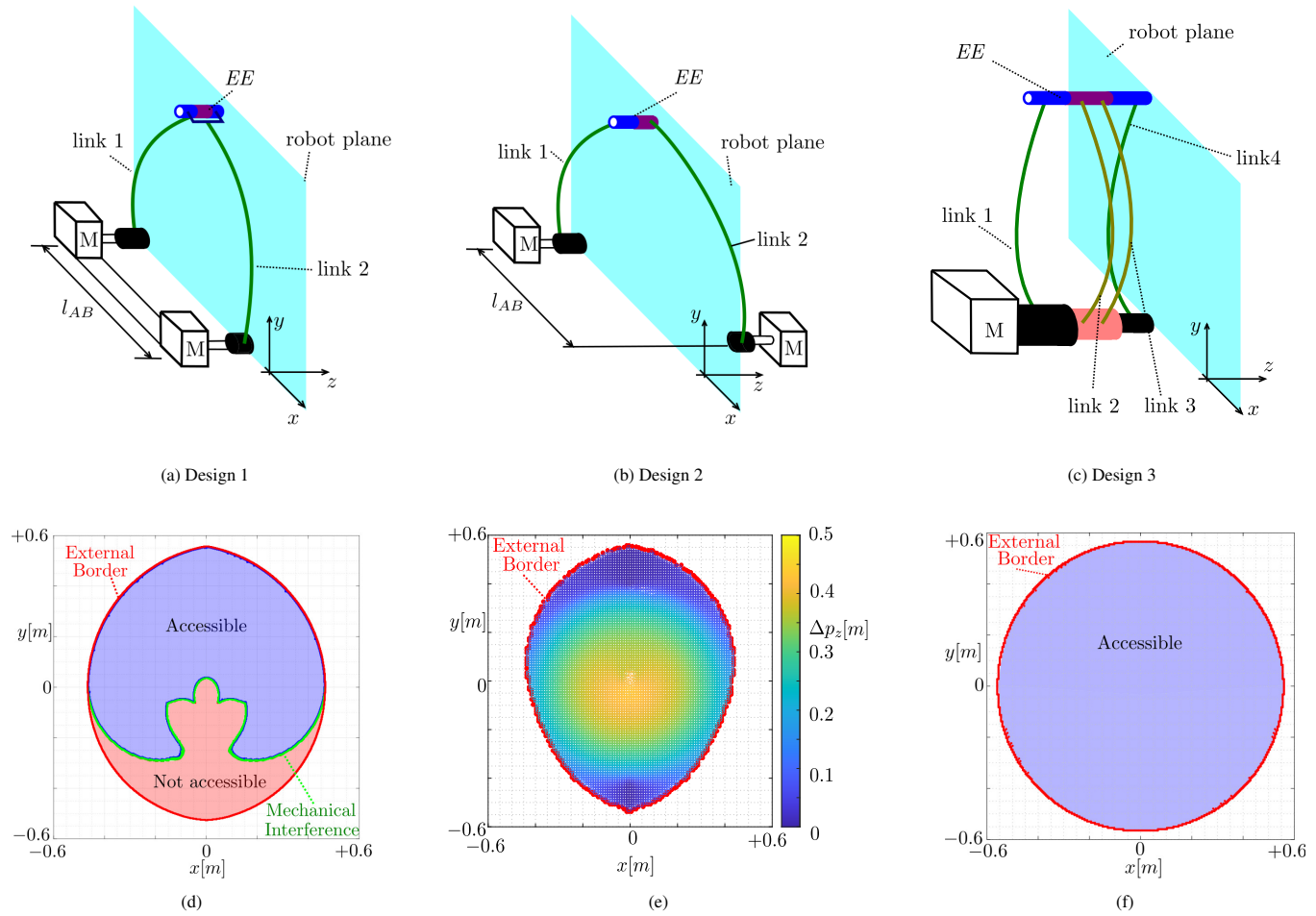


Figure 1: Three different possible designs of the $\underline{R}FRF\underline{R}$ robot. (a) two motors on the same side in distinct locations, (b) two motors on opposite sides on distinct locations, (c) two motors on the same side, same location. Figure (d) qualitatively illustrates how mechanical interference reduces the *WS* with Design 1. Figure (e) shows the trend of out-of-the-plane *EE* displacement ($\Delta p_z$) with Design 2, and (f) illustrates the *WS* with Design 3. The links length is 0.560 m, while $l_{AB}$ = 0.2 m for (d),(e), and $l_{AB}$ = 0 for (f).

*CPRs* workspace became of interest since their understanding may produce better-performing designs. At *WS* limits, *CPRs* may experience stable-to-unstable transition [26], analogously to serial *CRs* [27]. An optimal control approach was proposed in [26] to assess *CPRs* equilibrium stability, and experiments were conducted to verify the correct equilibrium stability prediction. Even though optimal control approaches bring rigorous derivation of equilibrium stability conditions, the complexity of the analysis is relevant. Conversely, discrete energy-based methods [28] bring simplicity to the equilibrium stability analysis.

The novel contribution of this paper is related to the experimental validation of *CPRs* equilibrium stability assessment. In particular, we demonstrate that models based on planar displacement assumptions may fail in the equilibrium stability prediction, even though the *CPR* is nominally planar. To this end, a *CPR* prototype for planar applications is originally proposed. The prototype has a $\underline{R}FRF\underline{R}$ overall topology [29], [30] and, thanks to its actuation system, links interference with each other is avoided throughout the robot *WS*, leading to a large attainable Cartesian *WS* area. Moreover, the *EE* motion is planar by design since the forces exchanged between the links and the *EE* are parallel to the motion plane, and the overall torque applied on the mechanism is normal to the motion plane. The robot capability in terms of joint-space range (*JS*), Cartesian *WS* size, and equilibrium stability (verified with the energetic approach of [28]) are compared by using a model that assumes planar displacements and a full spatial model. Experiments are conducted to i) verify that a model using planar displacements assumptions is not adequate to predict the equilibrium stability of the proposed prototype and ii) to assess the accuracy of our equilibrium stability prediction. A singularity type, related to out-of-the-plane uncontrolled motions of the planar *CPR*, is experimentally identified for the first time.

The paper is structured as follows. Section 2 illustrates the robot design and its prototyping. Then, Section 3 recalls the derivation of discretized *CPR* geometrico-static equations, singularity conditions and equilibrium stability assessment. Section 4 is devoted to the robot *JS*/*WS* analysis. Section 5 is dedicated to the experimental verification of equilibrium stability prediction, and conclusions are drawn in Section 6.

## 2. Prototype Design

This Section focuses on the $\underline{R}FRF\underline{R}$ prototype design proposed in this paper. The $\underline{R}FRF\underline{R}$ topology was introduced in [29], and its *WS* computation was studied in [30]. The $\underline{R}FRF\underline{R}$ robot has two rotative motors ($\underline{R}$) whose axes are attached to the proximal section of two flexible beams ($F$). The distal sections of the beams are connected through a passive revolute joint ($R$), and the robot *EE* is coincident with the passive revolute joint $R$. All the $R$ joint axes are nominally parallel.

### *2.1. Architecture Selection*

The proposed design aims at realizing a nominally planar *CPR* with the largest workspace possible. To keep planar the *EE* displacement, the external forces applied to the *EE* and the forces exchanged between the legs and the *EE* need to belong to the motion plane, with the resultant torque normal to the motion plane only. In addition, the *EE*, the links, and the motor axes should not mechanically interfere with each other: this feature is a great limiting factor for parallel robots *WS* size [31]. Some design candidates are the 2-*DoF* pick-and-place continuum robot of [9], and the $\underline{R}FRF\underline{R}$ of [6], but also many rigid-link five-bar mechanisms may be a source of inspiration [32]. The three most straightforward solutions are hereby discussed:

- Design 1 (Fig. 1a). The two $\underline{R}$ motors are attached on the same side of the working plane at a distance $l_{AB} > 0$. This design brings simplicity and great accessibility. Thanks to a clevis fastener, flexible links are aligned at the same *EE* cross-section and connected to the passive joint $\underline{R}$ [9], and the *EE* is in static equilibrium. However, mechanical interference between the links and motor shafts reduces the robot *WS*. We used the workspace algorithm of [33] to compute the *WS* boundaries generated by mechanical interferences, and a reduction of the *WS* to roughly half of the $xy$ plane occurs (Fig. 1d reports the robot *WS* obtained with $l_{AB} = 0.2$ m, links length 0.56 m and no external loads). Preliminary design explorations (not shown here for brevity) showed that the influence of mechanical interference reduces by lowering $l_{AB}$; on the other hand, $l_{AB}$ cannot be reduced to zero due to actuators encumberance;

- Design 2 (Fig. 1b). The two $\underline{R}$ motors are attached on the opposite side of the working plane at a distance $l_{AB} \geq 0$. The flexible beams are connected at different *EE* cross-sections (as [32], [6]), and there is no potential mechanical interference between robot links and motor axes. Unfortunately, the links wrenches will generate a resultant torque which is not normal to the motion plane, and the *EE* cannot lie in the nominal plane without additional constraining systems. We studied this phenomenon by computing the robot *WS* with a spatial robots model [34], and we measured the *EE* out-of-the-plane displacement $\Delta p_z$, namely the distance of the *EE* reference point from the reference motion plane. For instance, Fig. 1e illustrates $\Delta p_z$ over the robots *WS* in the case $l_{AB} = 0.2$, links length 0.56 m, no external loads and offset between the plane of the motors 0.020 m. When the *EE* points toward the *WS* centre, $\Delta p_z$ increases to unacceptable values. This issue may be solved by considering *EE*-constraining systems (e.g. the vaacum system of [35]). However, such a constraining system modifies the external actions acting on the robot. In this design, lowering $l_{AB}$ reduces $\Delta p_z$, but even with $l_{AB} = 0$, $\Delta p_z$ remains at unaccettable values. These simulations are not reported here for brevity;

- Design 3 (Fig. 1c). The two actuated revolute joints $\underline{R}$ are placed on the same side of the working plane, and they are coaxial ($l_{AB} = 0$). Flexible links 1 and 4 are synchronously moved by the same motor, whereas the other actuator rotates links 2,3. This design ensures no mechanical interference, the *EE* can maintain a planar configuration, ensuring a large accessible *WS* (Fig. 1f). However, the design complexity increases.

Design 3 is the most favourable for realizing a nominally planar 2-*DoF* system with the largest workspace, without requiring the addition of external constraints, and thus is selected for experiments.

### *2.2. Prototype Manufacture*

The proposed prototype is illustrated in Fig. 2. To facilitate its description, we can subdivide the robot into three groups: flexible chains, the *EE*, and the actuation unit.

The beams that transmit the motion from the actuators to the *EE* form the flexible chains. As represented in Fig. 2a, we can distinguish one inner and two outer chains. While four flexible beams make the former, each outer chain is made by two flexible beams. Beams are made of fibreglass rods of 2 mm diameter. Several possible materials are well suited for *CRs* (e.g. NiTinol alloys [4], Nylon [9], spring steel [24]), and we selected fibreglass mainly for its good tradeoff between lightweight, compliance, and widespread availability on the market. Even if a single beam of a larger diameter could be used to realize each flexible chain, we decided to use several beams in parallel. For a given flexural inertia moment, a single beam with a larger diameter is highly stressed since strains are proportional to the cross-section diameter. Instead, many small-diameter beams may guarantee an equivalent inertia moment, but the strain on each beam is reduced. We also mounted connecting constraints on each chain to increase the stiffness of the robot in the orthogonal direction to the working plane. This way, each flexible chain resembles a beam with a rectangular cross-section[1].

The *EE* is illustrated in Fig. 2b. The distal sections of the kinematic chains are connected to rigid clamps, as is done for the proximal section. The inner chain is clamped at the *EE* on $E_A$, while outer chains are connected to $E_B$,$E_C$. Two marker supports are attached at both sides of the *EE* to balance the *EE* load statically. The total mass of the *EE* is 218 g.

[1] A single beam with a rectangular cross-section would be a good design solution, but the market availability of beams with rectangular cross-section whose constitutive material has high admissible strains is significantly lower than circular beams.

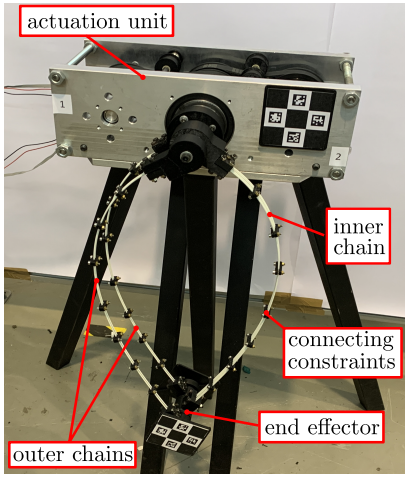


(a) Overview of the prototype

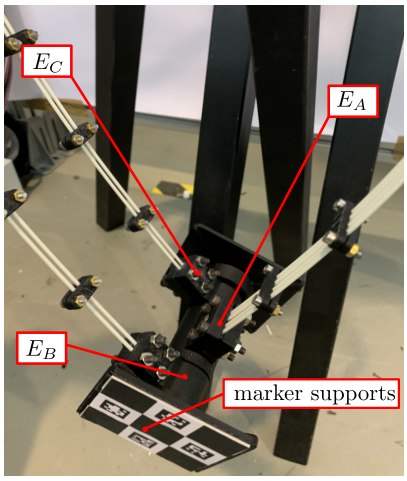


(b) End effector

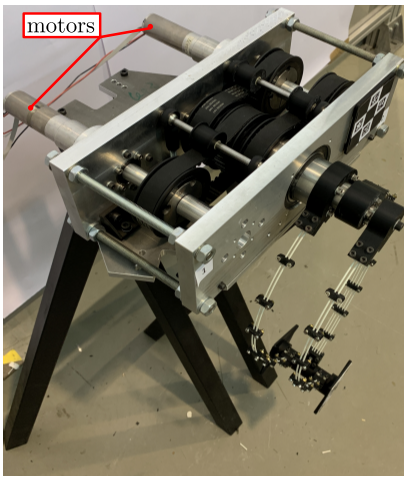


(c) Actuation unit

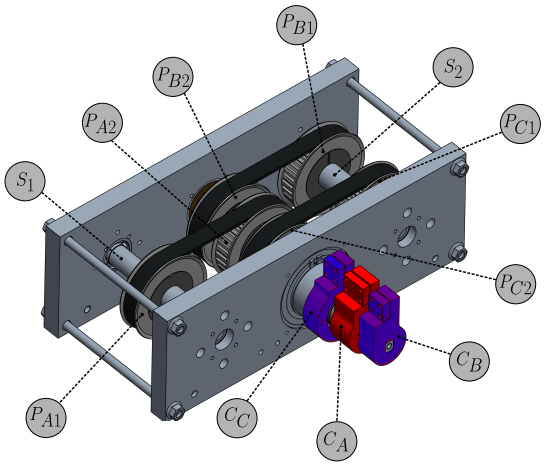


(d) Transmission system assonometric view.

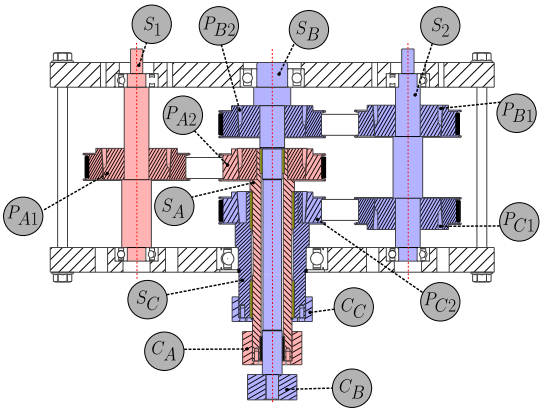


(e) Transmission system cross-section.

Figure 2: The *CPR* prototype is shown in (a), a top view of the prototype is given in (b) to highlight the actuation unit, and a view of the *EE* is provided in (c). Then, (d) provides an assonometric view of the transmisison system, and (e) illustrates a cross-section of the actuation unit: components that rotate at the same angular velocity are shaded with the same colour.

The actuation unit (Fig. 2c) is composed of Two DC Maxon motors DCX32L, equipped with a three-stage planetary gearbox (reduction ratio 150:1), and a transmission system specifically designed to drive the flexible chains according to Design 3. The transmission working principle is the following (see Fig. 2d): a rotation of the shaft $S_1$ causes an angular displacement of pulley $P_{1A}$. A synchronous belt transmits the rotation of $P_{1A}$ to the pulley $P_{2A}$. Similarly, shaft $S_2$ actuates pulleys $P_{1B}, P_{1C}$ and synchronous belts transmits the rotations to pulleys $P_{2B}, P_{2C}$, respectively. A set of three concentric shafts (see Fig. 2e) is used to transmit the rotation of the pulley to the beam clamps (named $C_A, C_B, C_C$). Shaft $S_A$ connects pulley $P_{2A}$ to $C_A$ and, in a similar fashion, shafts $S_B, S_C$ connects pulleys $P_{2B}, P_{2C}$ to $C_B, C_C$, respectively. Since $P_{2B}, P_{2C}$ rotate synchronously, also $C_B, C_C$, display the same angular motion. The proximal section of the inner chain is installed on $C_A$, while the proximal sections of the outer chains are placed at $C_B, C_C$.

Finally, a dSPACE 2018-B board completes the automation, controlling the DC motors.

## 3. Modelling

This Section briefly describes the energy-based modelling approach employed in this paper. We focus on the description of a spatial *CPR* model, which is the most general, and additional details on how to simplify it to a planar one can be found in Section 3.3. Let us consider an initially straight slender beam of length $L$, and $s$ is the curvilinear coordinate that spans $[0, L]$ (Fig. 3a). $\mathcal{F}_0$ is a fixed frame, and the pose of each reference frame $\mathcal{F}_s$, which is attached to each cross-section of the beam in its centre, can be represented as:

$$\mathbf{g}(s) = \begin{bmatrix} \mathbf{R}(s) & \mathbf{p}(s) \\ \mathbf{0} & 1 \end{bmatrix} \tag{1}$$

where $\mathbf{R} \in SO(3), \mathbf{p} \in \mathbb{R}^3$. The evolution of the beam pose over the $s$-coordinate is given by:

$$\mathbf{g}'(s) = \mathbf{g}(s)\hat{\boldsymbol{\xi}}(s) \tag{2}$$

with $(.)' = d/ds$, and $\hat{\boldsymbol{\xi}} \in se(3)$ is the skew-symmetric representation of the strain $\boldsymbol{\xi}(s) = [\mathbf{u}, \mathbf{v}] \in \mathbb{R}^6$, where $\mathbf{u}, \mathbf{v} \in \mathbb{R}^3$ are

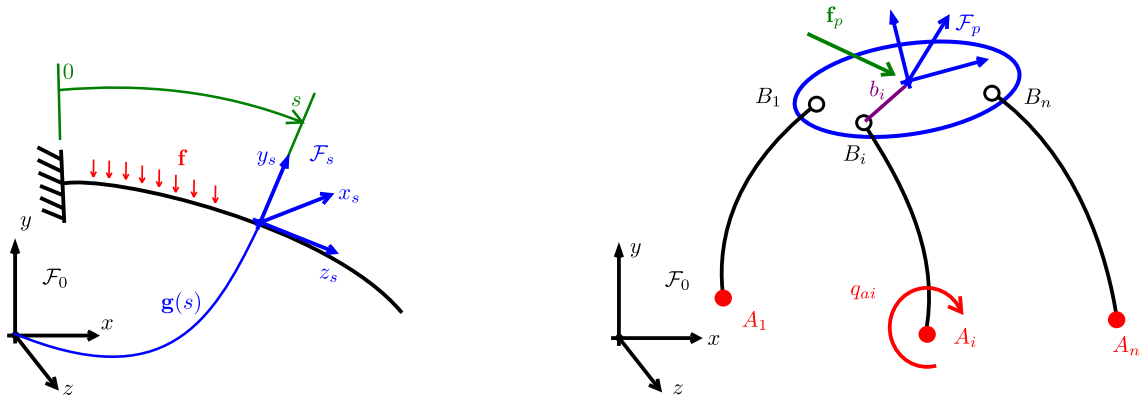


(a) Beam

(b) *CPR*

Figure 3: (a): flexible beam parametrization; (b) schematics of a *CPR*.

the angular and linear rate of change, respectively. Assuming that shear and extensibility are negligible and that the local $z$ axis is normal to the cross-section, we have $\mathbf{v} = \mathbf{e}_1 = [0, 0, 1]^T$. Material properties are considered linear, elastic, isotropic, and constant over the length, and only distributed forces $\mathbf{f} \in \mathbb{R}^3$ are applied over the beam. The total potential energy of the beam can be obtained as [36]:

$$V_{beam} = \int_0^L \left(\mathbf{u}(s)^T \mathbf{K}_{BT} \mathbf{u}(s) - \mathbf{f}^T \mathbf{p}(s)\right) ds \tag{3}$$

where $\mathbf{K}_{BT} = \text{diag}(K_x, K_y, K_z)$ is the local material stiffness matrix, $K_x, K_y$ are the flexural stiffness around the local $x_s, y_s$, and $K_z$ is the local torsional stiffness around $z_s$. In general, $K_x = EI_x, K_y = EI_y, K_z = GJ_z$, where $E$ is the Young's modulus, $G$ is the shear modulus, $I_x, I_y, J_z$ are the principal inertia moments of the cross-section.

Then, let us consider a *CPR* made by $n$ flexible beams (Fig. 3b): we assume each beam to be actuated at the proximal Section only (points $A_i$, with $i$ the index representing the $i$-th beam), $q_{ai}$ is the $i$-th actuated variable, and $\mathbf{q}_a \in \mathbb{R}^n$ collects the actuated variables. At the distal Section, a passive joint connects each flexible link to the rigid platform (points $B_i$). The frame $\mathcal{F}_p$ is attached to the rigid platform. Its pose is described by $(\mathbf{p}_p, \boldsymbol{\varphi}) \in \mathbb{R}^{n_c}$, where $n_c = 3$ for the planar case, $n_c = 6$ for the spatial case, and $\mathbf{p}_p, \boldsymbol{\varphi}$ represent the position and the orientation parameters of the platform w.r.t. $\mathcal{F}_0$, respectively. Assuming to have the same number of controlled and actuated variables, the vector $\mathbf{q}_p \in \mathbb{R}^n$ is introduced to stack the controlled variables, which is usually a subset of $\mathbf{p}_p, \boldsymbol{\varphi}$. Last, we introduce $\mathbf{q}_u \in \mathbb{R}^{n_c - n}$ to collect the remaining non-controlled platform-pose variables. The total potential energy of the *CPR* is obtained as:

$$V_{tot}(\mathbf{q}_a, \mathbf{q}_e, \mathbf{q}_u, \mathbf{q}_p) = \sum_{i=1}^{n} V_{beam_i} + V_{plat} \tag{4}$$

where $V_{plat} = -\mathbf{f}_P^T \mathbf{p}_p$, and $\mathbf{f}_P$ a platform load constant w.r.t. the fixed frame. Three-dimensional moments that are non-conservative are considered to not appear.

*CPRs* equilibrium configurations can be found by imposing that $V_{tot}$ is stationary [28]. A straightforward way to find critical points of $V_{tot}$ is to apply discretization strategies [11], and a finite set of discretization coordinates $\mathbf{q}_e$ is introduced to parametrize the elastic deformations of the beams. In this paper, we decided to employ the assumed strain mode discretization approach of [34], since it ensures a good trade-off between accuracy and computational time. The assumed strain mode approach is based on the discretization of $\mathbf{u}_i$ of the $i$-th beam through base functions as [37]:

$$\mathbf{u}_i(s) \simeq \mathbf{N}(s)^T \mathbf{q}_{ei} \tag{5}$$

where $\mathbf{N} \in \mathbb{R}^{3 \times N_f}$ is a matrix of base functions (such as orthogonal Legendre polynomials [34]), $N_f$ is the number of variables that discretizes $\mathbf{u}_i$, $\mathbf{q}_{ei} \in \mathbb{R}^{N_f}$ is the vector of the discretization variables of the $i$-th beam, and $\mathbf{q}_e \in \mathbb{R}^m, m = n(3 \times N_f)$ contains all the discretization variables. Then, to recover $\mathbf{g}$ at each $s$, we numerically integrate Eq. (2). where $\hat{\boldsymbol{\xi}}$ is build by considering the approximated strain as in Eq. (5). Consequently, after the discretization process, $V_{tot} = V_{tot}(\mathbf{q}_a, \mathbf{x})$, with $\mathbf{x} = [\mathbf{q}_d, \mathbf{q}_p], \mathbf{q}_d = [\mathbf{q}_e, \mathbf{q}_u]$, and a robot configuration is an equilibrium configuration if, for a fixed value of $\mathbf{q}_a$, $\mathbf{x}$ is a critical point of $V_{tot}$ [38]. However, due to the closed-loop architecture of *CPRs*, variables are related by geometric constraints, here denoted as $\boldsymbol{\Phi} = \boldsymbol{\Phi}(\mathbf{q}_a, \mathbf{x}) = \mathbf{0} \in \mathbb{R}^{n_\phi}$ without loss of generality[2]. In this case, critical point of $V_{tot}$ are characterized by Lagrange conditions [38]: $\mathbf{x}$ is a critical point of $V_{tot}$ if, assuming $\nabla_{\mathbf{x}} \boldsymbol{\Phi}$ full rank, there exists a vector of Lagrange multipliers $\boldsymbol{\lambda} \in \mathbb{R}^{n_\phi}$ such as:

$$\begin{cases} \nabla_{\mathbf{x}} \mathcal{L} = \nabla_{\mathbf{x}} V_{tot} + \nabla_{\mathbf{x}} \boldsymbol{\Phi}^T \boldsymbol{\lambda} = \mathbf{0} \\ \nabla_{\boldsymbol{\lambda}} \mathcal{L} = \boldsymbol{\Phi} = \mathbf{0} \end{cases} \tag{6}$$

with $\mathcal{L} = V_{tot} + \boldsymbol{\Phi}^T \boldsymbol{\lambda}$. Equation (6) is an undetermined system of $m + n_c + n_\Phi$ equations in $m + n + n_c + n_\Phi$ unknowns that represents the geometrico-static model of a *CPR*. Geometrico-

[2] Additional details on how to derive $\boldsymbol{\Phi}$ can be found in [28], [34].

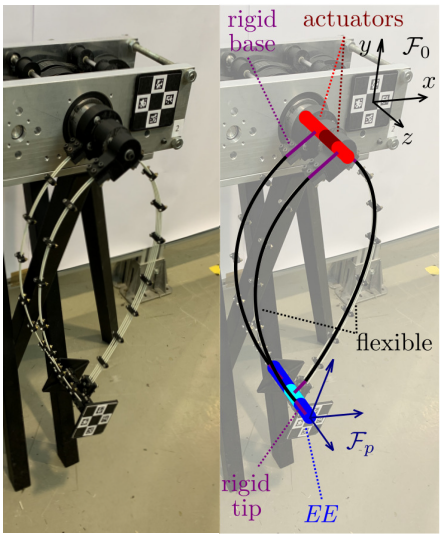


Figure 4: Schematics of the Prototype modelling

static problems[3] can be stated in an unified way as [28]:

$$\mathbf{F} = \begin{cases} \nabla_{\mathbf{x}} V_{tot} + \nabla_{\mathbf{x}} \mathbf{\Phi}^T \boldsymbol{\lambda} = \mathbf{0} \\ \mathbf{\Phi} = \mathbf{0} \\ \mathbf{e}_p = \mathbf{0} \end{cases} \tag{7}$$

where $\mathbf{e}_P = \mathbf{q}_p - \mathbf{q}_p^d$ for the inverse geometrico-static problem (*IGSP*), $\mathbf{e}_P = \mathbf{q}_a - \mathbf{q}_a^d$ for the forward geometric-static problem (*FGSP*), and the superscript $(.)^d$ denotes desired values. Both *IGSP* and *FGSP* are square systems of dimension $m+n+n_c+n_\Phi$ that can be solved thanks to nonlinear root-finding techniques. By using the assumed strain mode approach [34], $\mathbf{g}$ at each cross-section is obtained by numerical integration of Eq. (2). Thus, the terms of Eq. (7) that requires the derivative of $\mathbf{g}$ w.r.t. $\mathbf{x}$ are obtained by numerical integration of an additional set of ODEs, integrated together with Eq. (2). The expression of these terms is long, and its detailed description is not in the scope of this paper. We address the interested reader to a dedicated technical report [39].

### 3.1. Equilibrium Stability and Singularities

After the derivation of *FGSP* and *IGSP*, we seek to evaluate the equilibrium stability of the robot configuration and singularity conditions. To obtain singularity conditions, we linearize Eq. (6) at a generic equilibrium configuration [28]:

$$\begin{bmatrix} \mathbf{A}_\mathcal{L} \\ \mathbf{A}_\mathbf{\Phi} \end{bmatrix} \Delta\mathbf{q}_a + \begin{bmatrix} \mathbf{U}_\mathcal{L} \\ \mathbf{U}_\mathbf{\Phi} \end{bmatrix} \Delta\mathbf{q}_d + \begin{bmatrix} \mathbf{P}_\mathcal{L} \\ \mathbf{P}_\mathbf{\Phi} \end{bmatrix} \Delta\mathbf{q}_p + \begin{bmatrix} \mathbf{\Lambda}_\mathcal{L} \\ \mathbf{0} \end{bmatrix} \Delta\boldsymbol{\lambda} + \begin{bmatrix} \mathbf{W}_\mathcal{L} \\ \mathbf{0} \end{bmatrix} \Delta\mathbf{f}_p = \mathbf{0} \tag{8}$$

where:

1. $\mathbf{A}_\mathcal{L} = \nabla_{\mathbf{q}_a} (\nabla_{\mathbf{x}} \mathcal{L})$ , $\mathbf{U}_\mathcal{L} = \nabla_{\mathbf{q}_d} (\nabla_{\mathbf{x}} \mathcal{L})$
2. $\mathbf{P}_\mathcal{L} = \nabla_{\mathbf{q}_P} (\nabla_{\mathbf{x}} \mathcal{L})$ , $\mathbf{\Lambda}_\mathcal{L} = \nabla_{\boldsymbol{\lambda}} (\nabla_{\mathbf{x}} \mathcal{L})$ , $\mathbf{W}_\mathcal{L} = \nabla_{\mathbf{f}_P} (\nabla_{\mathbf{x}} \mathcal{L})$
3. $\mathbf{A}_\Phi = \nabla_{\mathbf{q}_a} \mathbf{\Phi}$ , $\mathbf{U}_\Phi = \nabla_{\mathbf{q}_d} \mathbf{\Phi}$ , $\mathbf{P}_\Phi = \nabla_{\mathbf{q}_P} \mathbf{\Phi}$

The terms of Eq. (8) requires the computation of the second derivatives of $\mathbf{g}$ w.r.t. $\mathbf{q}_a$ and $\mathbf{x}$. As for the first derivatives of $\mathbf{g}$ w.r.t. $\mathbf{x}$ of Eq. (7), also these terms are obtained by integration of an additional set of *ODEs* and the details on how the integration is carried out are reported in [39], for brevity sake.

For the singularity analysis, there is little interest in the variation $\Delta\boldsymbol{\lambda}$, since degeneracies of $\mathbf{\Lambda}_\mathcal{L}$ are unlikely to occur, in practice [28]. Being $\mathbf{Z}$ the matrix spanning the left nullspace of $\mathbf{\Lambda}_\mathcal{L}$ i.e. $\mathbf{Z}^T\mathbf{\Lambda}_\mathcal{L} = \mathbf{0}$, we eliminate $\Delta\boldsymbol{\lambda}$ by multiplying the first row of Eq. (8) by $\mathbf{Z}^T$:

$$\mathbf{A}\Delta\mathbf{q}_a + \mathbf{U}\Delta\mathbf{q}_d + \mathbf{P}\Delta\mathbf{q}_p + \mathbf{W}\Delta\mathbf{f}_p = \mathbf{0} \tag{9}$$

where:

$$\mathbf{A} = \begin{bmatrix} \mathbf{Z}^T\mathbf{A}_\mathcal{L} \\ \mathbf{A}_\mathbf{\Phi} \end{bmatrix}, \mathbf{U} = \begin{bmatrix} \mathbf{Z}^T\mathbf{U}_\mathcal{L} \\ \mathbf{U}_\mathbf{\Phi} \end{bmatrix}, \mathbf{P} = \begin{bmatrix} \mathbf{Z}^T\mathbf{P}_\mathcal{L} \\ \mathbf{P}_\mathbf{\Phi} \end{bmatrix}, \mathbf{W} = \begin{bmatrix} \mathbf{Z}^T\mathbf{W}_\mathcal{L} \\ \mathbf{0} \end{bmatrix} \tag{10}$$

To derive singularity conditions, the inverse and forward kinematostatic problems are established [28]. The inverse kinematostatic problem means to evaluate $\Delta\mathbf{q}_a, \Delta\mathbf{q}_d$ for given $\Delta\mathbf{q}_p, \Delta\mathbf{f}_p$, that is:

$$\begin{bmatrix} \Delta\mathbf{q}_a \\ \Delta\mathbf{q}_d \end{bmatrix} = -[\mathbf{A}\ \mathbf{U}]^{-1}(\mathbf{P}\Delta\mathbf{q}_p + \mathbf{W}\Delta\mathbf{f}_p) \tag{11}$$

Eq. (11) is solvable as long as $\mathbf{T}_1 = [\mathbf{A}\ \mathbf{U}]$ is full-rank, and rank deficiencies of $\mathbf{T}_1$ are named Type-1 singularities [28]. These singularities are related to limits of *IGSP* and impossible motions of $\mathbf{q}_p$. On the other hand, the forward kinematostatic problem means to evaluate $\Delta\mathbf{q}_p, \Delta\mathbf{q}_d$ for given $\Delta\mathbf{q}_a, \Delta\mathbf{f}_p$, that is:

$$\begin{bmatrix} \Delta\mathbf{q}_p \\ \Delta\mathbf{q}_d \end{bmatrix} = -[\mathbf{P}\ \mathbf{U}]^{-1}(\mathbf{A}\Delta\mathbf{q}_a + \mathbf{W}\Delta\mathbf{f}_p) \tag{12}$$

Eq. (12) is solvable as long as $\mathbf{T}_2 = [\mathbf{P}\ \mathbf{U}]$ is full-rank, and degeneracies of $\mathbf{T}_2$ are named Type-2 singularities [28] Robot configurations where $\mathbf{T}_2$ is degenerate are related to the limits of the *FGSP* solution and uncontrollable $\mathbf{q}_p$ motions. Then, we evaluate equilibrium stability by determining the reduced Hessian matrix $\mathbf{H}^r$ of the total potential energy as [28]:

$$\mathbf{H}^r = \mathbf{Z}^T \frac{\partial^2 \mathcal{L}}{\partial \mathbf{x}^2} \mathbf{Z} = \mathbf{Z}^T \begin{bmatrix} \mathbf{P}_\mathcal{L} & \mathbf{U}_\mathcal{L} \end{bmatrix} \mathbf{Z} \tag{13}$$

The configuration is stable if $\mathbf{H}^r$ is positive definite. Please note that, as long as $\mathbf{Z}$ is full rank, $\mathbf{T}_2$ is singular if and only if $\mathbf{H}^r$ is rank deficient (see [28] for the proof). Thus, Type-2 singularities are associated with the variation of the stability pattern.

### 3.2. Distributed Material Coefficients Computation

The specific design of the flexible chains needs to be accounted for in the robot model (Fig. 4). Each chain comprises a rigid base attached to the motor shaft, rigidly rotating with it, some flexible beams fixed to the motor shaft, several connecting constraints between the flexible beams, and finally another rigid tip attached to the *EE* revolute joint. As previously mentioned, connecting constraints increase the robot stiffness in the

[3] With *FGSP* we consider the evaluation of $\mathbf{q}_e, \mathbf{q}_u, \mathbf{q}_p, \boldsymbol{\lambda}$ for given external loads and assigned $\mathbf{q}_a$. On the other hand, the *IGSP* means the evaluation of $\mathbf{q}_e, \mathbf{q}_u, \mathbf{q}_a, \boldsymbol{\lambda}$ for given external loads and assigned $\mathbf{q}_p$.

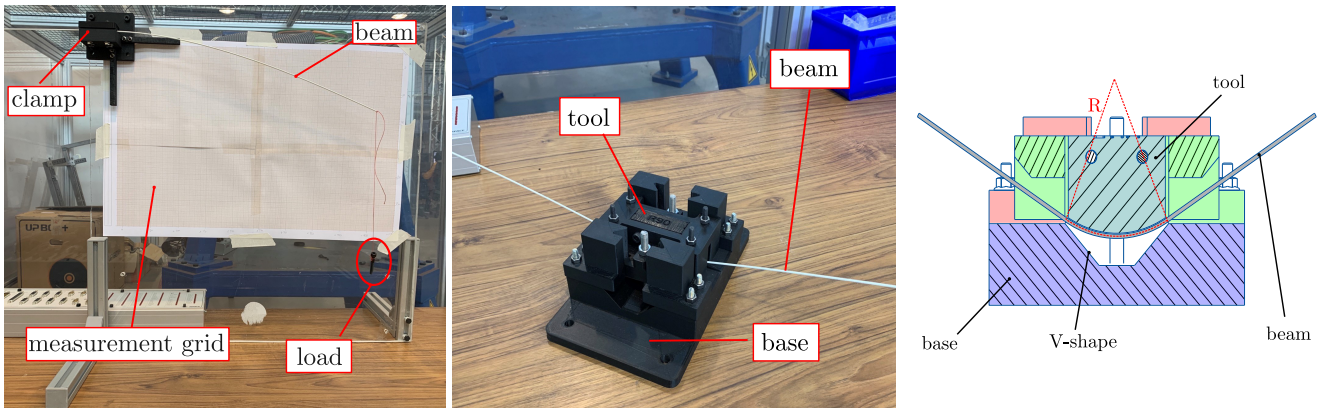


(a) Young's's modulus setup (b) Strain limit setup (c) Cross-secton of the strain-limit setup

Figure 5: Experimental benchmarks. Figure (a) illustrates the Young's's modulus estimation setup, Figure (b) shows the strain limit estimation setup and Figure (c) gives details on the strain limit estimation setup.

orthogonal direction to the motion plane. However, accounting for their effect in the robot model is not trivial. We can simulate each beam and each connecting constraint using the assumed mode approach [37], leading to computationally expensive models. Alternatively, other modelling strategies may be used: piecewise constant curvature approaches [40], or piecewise constant strains [41] fits well, but they may require a large number of elastic coordinates. Thus, we decided to consider each flexible chain as a single equivalent beam (Fig. 4) modelled using the assumed strain mode approximation [37]. In this way, we reduce the number of elastic variables in $\mathbf{q}_e$ necessary to represent the flexible chains while considering the effect of connecting constraints.

To represent each flexible chain as a single equivalent beam, we need to calculate an equivalent matrix $\mathbf{K}_{BT}$ (Eq. (3)) that represents the overall effect of several beams in parallel connected by connecting constraints. Assuming linear isotropic elasticity of the equivalent beam, we use rules of springs in series and in parallel to evaluate two flexural stiffness and the torsional modulus for each flexible chain. By proceeding in this way (see Appendix A for the mathematical derivation), we obtained:

$$\mathbf{K}_{BT-in} = EI\ \mathrm{diag}(4, 48n_b^2, 60n_b^2, h^2) \tag{14}$$

$$\mathbf{K}_{BT-out} = EI\ \mathrm{diag}(2, 24n_b^2, 12n_b^2, h^2) \tag{15}$$

where $\mathbf{K}_{BT-in}$ is the stiffness of the inner chain, $\mathbf{K}_{BT-out}$ is the stiffness of a single outer chain, $n_b$ is the number of segments, and $h$ is the distance between the beams, assumed to be equal for each of them. By looking at the expressions of Eqs. (15), it is clear that adding connecting constraints increases the robot stiffness in the direction orthogonal to the motion plane. Also, since we neglect the torsion that acts on each beam, the equivalent parameters depend on the Young's modulus only: this parameter should be identified appropriately to obtain accurate results.

### 3.3. Remarks on Planarity Assumptions

The proposed prototype (Fig. 2) is theoretically planar, and using a planar model to simulate it appears legitimate. A planar model brings mathematical simplicity and a reduced number of variables to be considered [42]. However, as we later show with experiments, a planar model neglecting out-of-the-plane phenomena is inadequate to assess equilibrium stability limits, and ultimately the workspace size. This Section highlights the most relevant differences between a spatial model and a planar *CPR* model.

Let us consider Fig. 3. For a prescribed *CPR* motion plane, a planar *CPR* model assumes that:

- the cross-section of each beam and the *EE* only perform planar displacements belonging to the reference plane;
- the cross-section of each beam and the *EE* rotate about an axis orthogonal to the reference plane;
- all the forces belongs to the reference plane, and all the torques are orthogonal to the said plane only;

Under these assumptions, the beams pose can be defined by $\mathbf{p}(s), \theta(s)$, namely the position and the orientation angle of the frame $\mathcal{F}_s$ w.r.t. $\mathcal{F}_0$, respectively. In this case, $\mathbf{g} \in SO(2)$ and $\boldsymbol{\xi} = [u, \mathbf{v}] \in \mathcal{R}^3$. The scalar quantity $u$ is the beam curvature and $\mathbf{v} = [1, 0] \in \mathbb{R}^2$ if shear and extensibility are negligible. The total potential energy of the beam $V_{beam}$ of Eq. (3) becomes:

$$V_{beam} = \int_0^L K_x u(s)^2 - \mathbf{f}^T \mathbf{p}(s) ds \tag{16}$$

It should be noted that the beams torsion and the out-of-the-plane curvature do not appear on $V_{beam}$ since the beams possible motions do not allow these deformations. Then, $\mathbf{p}_p \in \mathbb{R}^2, \theta_p \in \mathbb{R}$ describes the position and the orientation angle of $\mathcal{F}_p$ w.r.t. $\mathcal{F}_0$, respectively. $V_{tot}$ is obtained as in Eq. (4), and constraints equations are formalized as in a spatial model but with a lower dimension of $\mathbf{\Phi}$.

A major advantage of using a planar model is the reduced number of discretization variables employed. When using Eq. (5), $m = n(3 \times N_f)$ elastic coordinates are introduced to discretize $\mathbf{u}$ while, in a planar model, $u \in \mathbb{R}$ and $m = nN_f$. Then, Eq. (7) is formulated equivalently, but the number of equations reduces

since the dimension of $\mathbf{x}$ reduces. Singularity conditions and the equilibrium stability assessment are performed in the same fashion in a planar or spatial model but with different dimensions of $\mathbf{T}_1, \mathbf{T}_2$ and $\mathbf{H}_r$.

## 4. Robot Analysis

In this Section, we focus on material characterization and *JS*/*WS* evaluation of the proposed prototype. To obtain accurate *JS*/*WS* predictions, model parameters should be identified appropriately. While robot geometric parameters can be directly measured with limited uncertainty, material parameters are affected by a greater variability. Therefore, the following subsection focuses on material parameters calibration.

### *4.1. Material Characterization*

It is well known from material science that standardized tests for fibreglass may be conducted to evaluate the Young's modulus $E$, and the strain limit $\epsilon_{max}$ [43]. These experimental setups require complex and expensive equipment that may not be available. On the other hand, a simple model-based bending test may be conducted for flexible beams to identify at least $E$ [3], [44], [45]. In this test, a clamped beam is subjected to several known loading conditions, and the Young's modulus is selected as the one that minimizes the error between model predictions and experimental measures (Fig. 5a). To this end, $n_L$ loads are applied to the tip of a clamped beam. Being $j = 1, \cdots, n_L$ the index representing the $j$-th different load condition, $\mathbf{p}_{ej}$ is the experimentally measured tip deflection, and $\mathbf{p}_{mj}$ the model predicted tip position, which depends on $E$. The Young's modulus is found by solving the nonlinear least squares problem [45]:

$$E = \text{argmin}_E \sum_{j=1}^{n_L} \|\mathbf{p}_{mj} - \mathbf{p}_{ej}\|_2^2 \tag{17}$$

or, equivalently, as the solution of the following nonlinear equations:

$$G(E) = \frac{\partial}{\partial E} \sum_{j=1}^{n_L} \|\mathbf{p}_{mj} - \mathbf{p}_{ej}\|_2^2 = 2 \sum_{j=1}^{n_L} \left(\mathbf{p}_{mj} - \mathbf{p}_{ej}\right)^T \mathbf{J}_{mj} = 0 \tag{18}$$

with $\mathbf{J}_{mj} = \frac{\partial \mathbf{p}_{mj}}{\partial E}$. The terms $\mathbf{p}_{mj}, \mathbf{J}_{mj}$ depend on the selected beam model: in this work, $\mathbf{p}_{mj}$, and $\mathbf{J}_{mj}$ are obtained thanks to the use of the assumed strain mode approach of [37], but their expression is not reported for brevity. We performed the Young's's modulus evaluation with ten different beams, and each beam was subjected to $n_L = 20$ different load conditions. As shown in Fig. 5a, a known tip load was applied to the beam, and the corresponding tip position $\mathbf{p}_{ej}$ was measured with a measurement grid. The resulting Young's's modulus was determined as $E = 36.1$ GPa, in agreement with the provider range of [25, 40] GPa.

Since measurement errors may potentially influence the calibrated value, we propose a methodology to estimate how a measurement error is reflected on the calibrated $E$. Being $\mathbf{p}_{mes} = [\mathbf{p}_{m1}, \cdots, \mathbf{p}_{mi}, \cdots \mathbf{p}_{mn}] \in \mathbb{R}^{2n_L}$ the vector that collects the measurements, linearizing Eq. (18) yields:

$$\frac{\partial G}{\partial E} dE + \frac{\partial G}{\partial \mathbf{p}_{mes}} d\mathbf{p}_{mes} = 0 \tag{19}$$

with:

$$\frac{\partial G}{\partial E} \in \mathbb{R} \; ; \; \frac{\partial G}{\partial E} = 2 \sum_{i=1}^{n_L} \left( \mathbf{J}_{mi}^T \mathbf{J}_{mi} + (\mathbf{p}_{mi} - \mathbf{p}_{ei})^T \frac{\partial \mathbf{J}_{mi}}{\partial E} \right) \tag{20}$$

$$\frac{\partial G}{\partial \mathbf{p}_{mes}} \in \mathbb{R}^{1 \times 2n_L} \; ; \; \frac{\partial G}{\partial \mathbf{p}_{mes}} = -2 \left[\mathbf{J}_{m1}, \cdots, \mathbf{J}_{mi}, \cdots, \mathbf{J}_{mn}\right] \tag{21}$$

By further manipulations, we get:

$$dE = -\left(\frac{\partial G}{\partial E}\right)^{-1} \left(\frac{\partial G}{\partial \mathbf{p}_{mes}}\right) d\mathbf{p}_{mes} = \mathbf{W} d\mathbf{p}_{mes} \tag{22}$$

The matrix $\mathbf{W} \in \mathbb{R}^{1 \times 2n_L}$ correlates $dE$ to $d\mathbf{p}_{mes}$, Assuming $\mathbf{W}$ as deterministic, and assuming each component of $\mathbf{p}_{mes}$ to be affected of a measurement error with normal distribution $\mathcal{N}(0, \sigma_x^2)$, the Young's modulus error follows a normal distribution $\mathcal{N}(0, \sigma_E^2)$, where $\sigma_E$ [46]:

$$\sigma_E = \sqrt{\mathbf{W}\mathbf{W}^T} \sigma_x = w \sigma_x \tag{23}$$

By considering the measurements used for the Young's modulus calibration, we obtained $w = 12.3 \cdot 10^{-2} \frac{GPa}{mm}$, and $w$ represent how a measurement error is projected on a variation of the calibrated $E$. For instance, a measurement error of 2 mm (which is realistic with the employed methodology) results in a variation of 0.246 GPa of $E$, which is less than 1% of the computed values of $E$. Thus, the simple methodology employed fits the system at hand, which would not significantly benefit from more accurate tip position measurements.

The second material parameter to be evaluated is the strain limit $\epsilon_{max}$, which will be used during the *JS*/*WS* evaluation to verify that no leg rupture will occur. As before, instead of performing standard tests, we propose a simplified procedure that can be easily reproduced for fragile materials. The setup is represented in Fig. 5b: a flexible beam of radius $r$ is placed between a V-shaped component and a tool with a circular tip of radius $R$ (see Fig. 5c). The tool is pressed onto the beam, which then assumes the same curvature of the tool $u = 1/R$, where pressed. Therefore, the strain on the constant curvature portion is:

$$\epsilon = ru = \frac{r}{R} \tag{24}$$

To estimate $\epsilon_{max}$, we test the beam with several tools characterized by decreasing $R$ until a brittle fracture of the beam occurs. Then, the last value of $R$ where the beam deforms without damage is used to compute $\epsilon_{max}$ with Eq. (24). We performed this procedure with the same beams used for the Young's modulus calibration, and we obtained $\epsilon_{max} = 2.75\%$, which is in accordance with the provider specification of $\epsilon_{max} \geq 2\%$. Please also note that the simplified procedure we proposed ensures an underestimation of the real $\epsilon_{max}$: a finite number of tools is used,

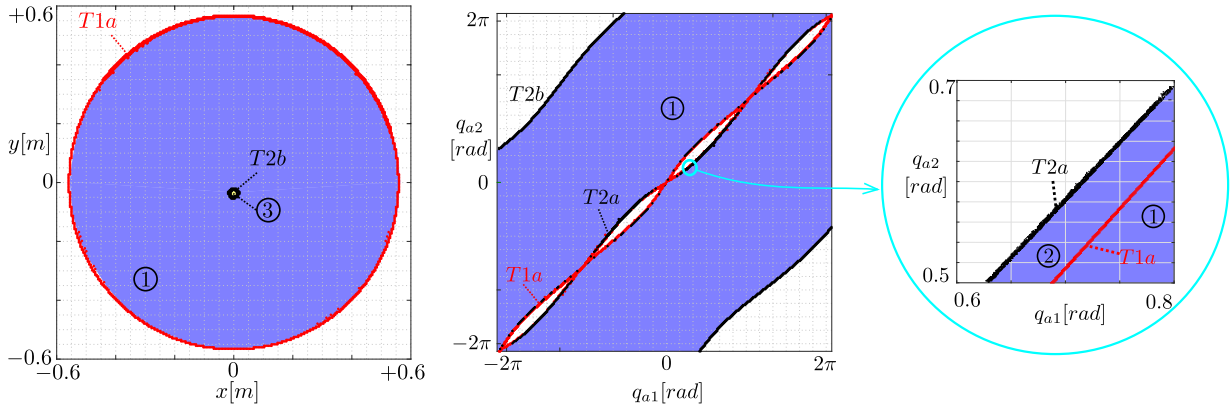


(a) Cartesian Workspace, planarity assumptions.

(b) Jointspace Range, planarity assumptions.

Figure 6: Jointspace and Cartesian workspace obtained by using planar displacements assumptions. The Cartesian workspace is represented in (a), and the jointspace in (b). Stable and unstable configurations are depicted in blue and yellow, respectively. Type-1 singularities are shown in red and Type-2 singularities in black.

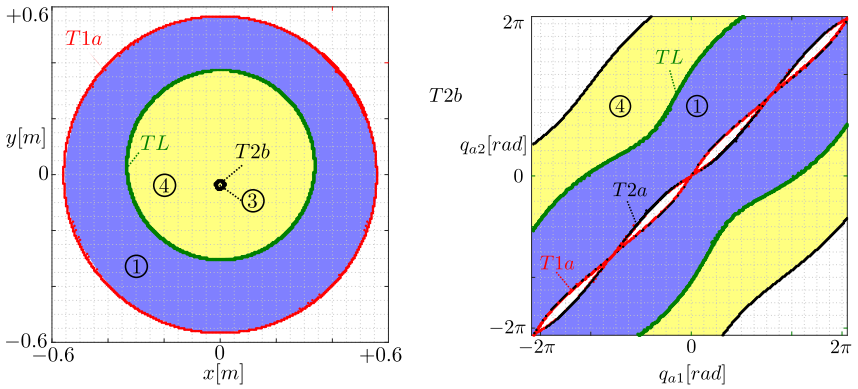


(a) Cartesian Workspace, full spatial model.

(b) Jointspace Range Magnification, full spatial model.

Figure 7: Jointspace and Cartesian workspace obtained using a full spatial model. The Cartesian workspace is represented in (a), and the jointspace in (b). Stable and unstable configurations are depicted in blue and yellow, respectively. Type-1 singularities are shown in red and Type-2 singularities in black. Singularities, where **U** is degenerate, are plotted in green.

and the exact $\epsilon_{max}$ is only approximated by the last value of $\epsilon$ where the beam deforms without damage. In the case more accurate characterization of $\epsilon_{max}$ is required, which is not our case; standard tests are recommended [43].

### *4.2. Joint space and Cartesian workspace Analysis*

Once the robot model is established and the material parameters identified, we can evaluate the robot motion capabilities in terms of *JS*/*WS* computation. The flooding algorithm of [30] is used for this scope: the flooding algorithm is an explorative algorithm based on a grid discretization of the target space (e.g. the *JS* or *WS*). Several phenomena define the *JS*/*WS* limits and by using the flooding algorithm, we considered:

- Singularities. As explained in Section 3, singularities define the *JS*/*WS* boundaries. A configuration is considered singular if the inverse condition number of $\mathbf{T}_1$ or $\mathbf{T}_2$ is below a defined threshold ($10^{-5}$ in our case)[4];
- Equilibrium stability. We checked stability by looking at the positive definiteness of $\mathbf{H}^r$;
- Strain limits on the flexible links: we evaluate if the strain on each leg does not exceed $\epsilon_{max} = 2.75$ %.

The results of the *JS* and *WS* of our prototype are reported in Figs. 6,7. We performed our evaluation by considering planar displacement assumptions (Fig. 6) and by using a full spatial model (Fig. 7). The discretization through assumed mode is performed by using four modes on each allowed deformation mode, and thus $m = 12 \cdot 2$ legs for the spatial model and $m = 4 \cdot 2$ legs for the planar model. Gravitational loads such as *EE* weight and beams distributed weight are considered. No configuration exceeded the strain limit of $\epsilon_{max} = 2.75$ %.

First, let us consider the case where planar displacements assumptions are introduced in the robot model: Fig. 6a illustrates the *WS*, and Fig. 6b the *JS*. Region ① is a region where the robot assumes stable configurations. Singularity curve $T1a$, that is, a Type-1 singularity where $\mathbf{T}_1$ is degenerate with **A** and **U** full rank, delimits ① from one side and represent the external *WS* boundary (Fig. 6a): there is no solution to the *IGSP* at each point of $T1a$, and the robot *EE* cannot exceed $T1a$ with

[4]Matrix $\mathbf{T}_1, \mathbf{T}_2$ have nonhomogeneous units: the use of the inverse condition number is valid as long as we intend to detect the degeneracy of the corresponding matrices, and not to analyze robots performances.

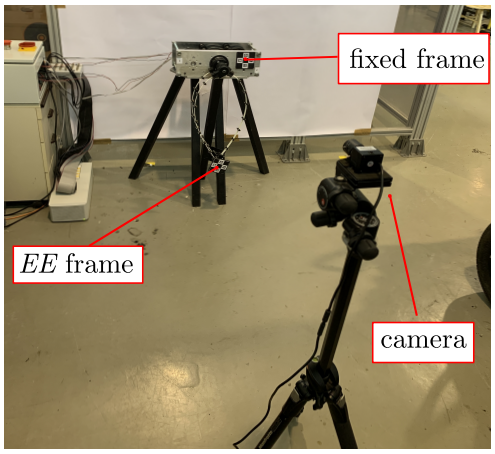


Figure 8

imposed *EE* position. Singularity curve $T2a$ is a Type-2 singularity where $\mathbf{T}_2$ is degenerate with $\mathbf{P}$ and $\mathbf{U}$ full rank, and it defines the inner *JS* limits (Fig. 6b): at each point of $T2a$ there exists no static solution to the *FGSP* and, by crossing $T2a$, the robot equilibrium becomes unstable [28]. Between $T1a$ and $T2a$, there exists a small stable region named ② (magnified in Fig. 6b) where the robot equilibrium is stable. These configurations can be reached by commanding the robot joints, but region ② cannot be reached by imposing the *EE* position since $T1a$ cannot be crossed with imposed *EE* position. On the other side, the singularity curve $T2b$, which delimits the *JS* limits, is a parallel singularity where $\mathbf{T}_2$ is singular. Singularity curve $T2b$ encircles a small *WS* region named ③ where the robot equilibrium is unstable[5].

Second, we now consider the case where a full spatial model is used: the *WS* and the *JS* are illustrated in Fig. 7a, Fig. 7b, respectively. We can observe that singularity curve $T1a, T2a, T2b$ are equally predicted by a model with planar displacement assumptions and by a full spatial model. **However**, the use of a full spatial model reveals an additional singularity curve named $TL$, which is a curve where both $\mathbf{T}_1$ and $\mathbf{T}_2$ are singular because $\mathbf{U}$ is singular. The singularity curve $TL$ defines a new region ④, where the spatial model predicts an unstable equilibrium, and the extension of the stable region ① is consequently reduced.

For each point inside ④, both planar and spatial model predicts the same robot configuration in terms of $\mathbf{q}_a, \mathbf{x}$, but the equilibrium stability is predicted differently. This discrepancy between a model with planar displacement assumptions and a full spatial model is remarkable and, to the best of our knowledge, identified for the first time in *CPRs*. Thus, experiments are conducted to verify which simulation prediction is realistic.

## 5. Experiments

The aim of this Section is to experimentally validate the analysis conducted in Sec. 4 about the *JS*/*WS* prediction of the proposed prototpe. We first address the question of whether a model with planar assumptions is adequate to model our prototype or not. Then, we focus on the experimental reconstruction of singularity curves that delimits the prototype range of motions, namely $T2a$ and $TL$. For each curve, we compare simulation with experimental data to assess the accuracy of our prediction.

To acquire experimental data, we employed the experimental setup illustrated in Fig. 8. A fixed camera was used to record images of the Charuco Board marker attached to the *EE*, and these pictures were then processed using an OpenCV Python library [47] to reconstruct the *EE* pose. For each reconstructed pose of the *EE*, the motors' angular position was also logged, assuming the motors' PID controller steady-state error to be negligible.

### 5.1. JS and WS verification

In this subsection, we verify the correctness of the *JS*/*WS* simulation we performed in Sec. 4. To do this, we move the robot in several stable configurations with *EE* positions equally distruibuted over the *WS*, and we store motor angles and *EE* position at each configurations. We also seek to reach exterior *WS* limits, by moving the *EE* as far as possible from the motor axis, and inner *WS* limits, by moving the *EE* toward the motor axis.0 Figure 9 displays the superimposition between experimental data and simulations. Experimental joint angles are superimposed over the computed *JS*, while measured *EE* positions over the theoretical *WS*. The model with planar displacements assumptions is used in Figs. 9a,9b and the full spatial model is employed in Figs. 9c,9d.

By looking at Fig. 9, we observe that experimental data qualitatively agrees with the simulations obtained by using a full spatial model is used, while the experiments are in disaccordance with a model that employs planar displacement assumptions. In particular, we can state that the stable motion capabilities of the robot are delimited by singularity curves $T2a, TL$. While $T2a$ is equally predicted by both models, $TL$ is only visible by using a full model. We may find an analogy between these singularities and the constraint singularities appearing in rigid-link lower-mobility parallel robots [48]. For these robots, constraint singularities do not appear in the reduced kinematics model which neglects the possibilities of the robot platform to move along certain (*a priori*) constrained directions of the space. They may be found if and only if the complete static-equilibrium model, allowing all possible motions in 3D, is analyzed. Analogously to what happens for these constraints singularities, singularities characterized by the curve $TL$ in the present work may be observed if and only if the full (spatial) kinemato-static model of the robot is analyzed.

In the next Sections, we are going to separately investigate $T2a$ and $TL$ curves, to understand the physical phenomena happening when crossing singularities, and to assess the accuracy of our equilibrium stability reconstruction.

### 5.2. Exterior WS boundary

The exterior *WS* boundary is defined by singularity curve $T2a$, that is a Type-2. As theorized in [28], Type-2 singular-

[5] Since $T_2$ defines the *JS* limits, ③ is not visible in Fig.6b

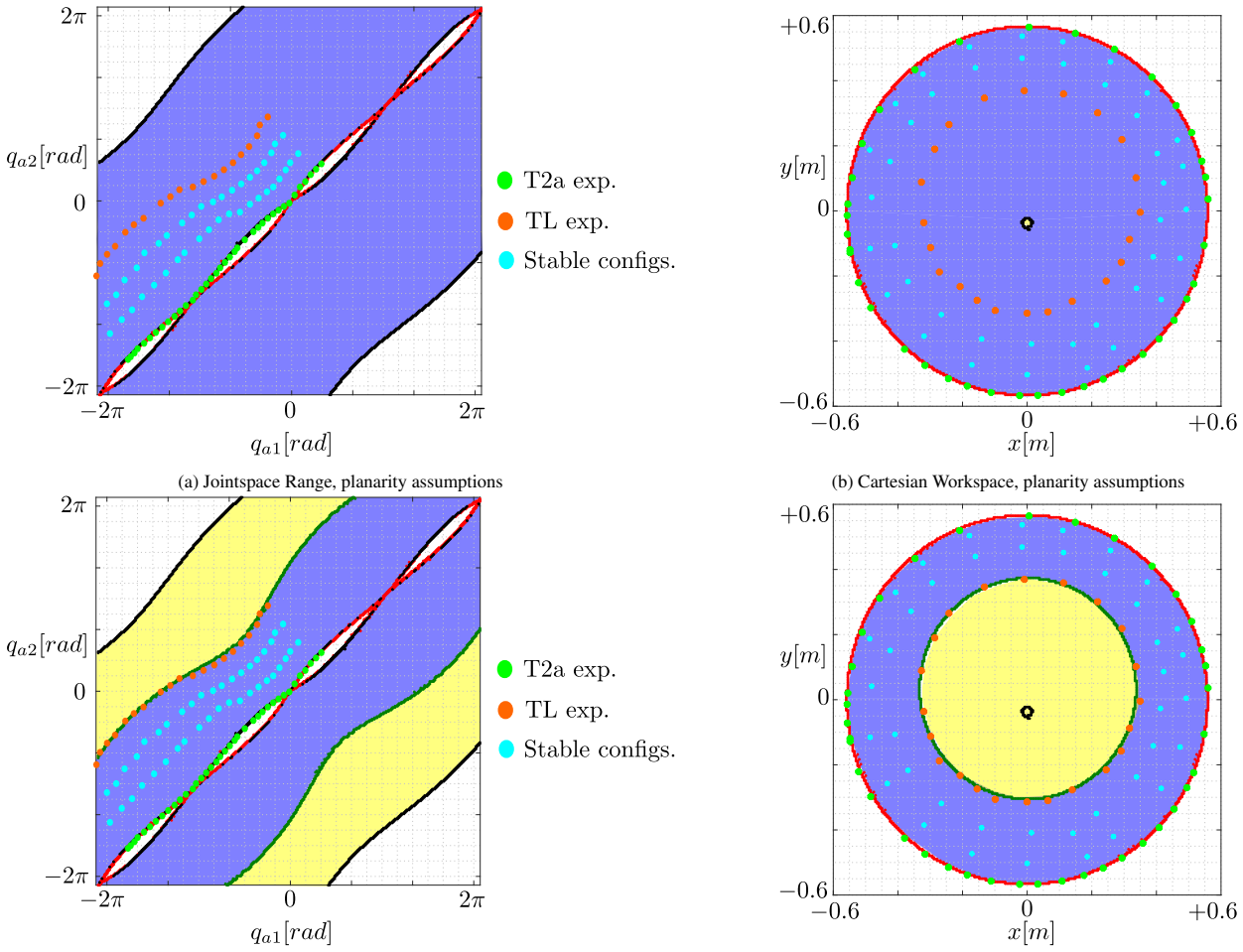


(a) Jointspace Range, planarity assumptions

(b) Cartesian Workspace, planarity assumptions

(c) Jointspace Range, full spatial model

(d) Cartesian Workspace, full spatial model

Figure 9: Superimposition between theoretical and experimental data. Results for the model with planar displacement assumptions are reported in (a) for the jointspace range (a) and (b) the Cartesian workspace. Then, the jointspace range and the Cartesian workspace obtained with a full model are reported in (c), and (d), respectively. Stable and unstable configurations are depicted in blue and yellow, respectively. Type-1 singularities are shown in red and Type-2 singularities in black. Singularities, where **U** is degenerate, are plotted in green.

ity delimits stable-to-unstable transitions. In particular, we experimentally observed that $T2a$ is associated with a snapping phenomenon (see accompanying video at min.0 sec.7). When quasi-statically reaching a singular configuration, a non-null motion of the *EE* occurs even though the motors are braked, and the robot dynamically snaps, as shown in Fig. 10. The snapping motion occurring about the $T2a$ curve belongs to the motion plane: this is reasonable since both planar and spatial models equally predicted the phenomenon. To reconstruct the $T2a$ curve, we placed the robot in stable configurations as close as possible to the stability limit. The motor angles are slowly adjusted to move near $T2a$, aiming not to cross it. Once the robot snaps, the joint values and the Cartesian configuration prior to snapping are recorded as a *JS* or *WS* border points. Some examples of these configurations near the $T2a$ are depicted in Figs. 11a,11b,11c.

To assess the accuracy of our equilibrium stability prediction, we tested 38 different configurations near $T2a$, with *EE* positions equally distributed over the *WS*. For each test, we name $\mathbf{q}_{exp}, \mathbf{p}_{exp}$ the experimental motor angle, and the camera-acquired *EE* position where the singularity happens, respectively. We also introduce $\mathbf{q}_t$ that is the theoretical motors angles where the instability should happen: $\mathbf{q}_t$ is defined as the point that lies over $T2a$ closest to $\mathbf{q}_{exp}$. Finally, we define $\mathbf{p}_t$ as the Cartesian point that corresponds to $\mathbf{q}_t$ (see Fig. 12 for a graphical illustration). For each configuration, we define:

$$e_q = \|\mathbf{q}_{exp} - \mathbf{q}_t\|_2 \tag{25}$$

$$e_p = \|\mathbf{p}_{exp} - \mathbf{p}_t\|_2 \tag{26}$$

where $e_q, e_p$ are named motor angles error and *EE* position error, respectively. Table 1 summarizes the results: a mean $e_q = 2.68°$ is obtained, which corresponds to a mean $e_p = 23,13$ mm (4.10 % w.r.t. total link length of 564mm).

The causes of error are numerous: hardware inaccuracies (e.g., friction, belt elasticity, gearbox clearance) and model errors (such as parameter uncertainties, distributed parameter assumption, and discretization inaccuracy). To investigate the discretized model errors, we compute $\mathbf{p}_m$, that is the *EE* position obtained by solving the *FGSP* with motor angles $\mathbf{q}_{exp}$ (see

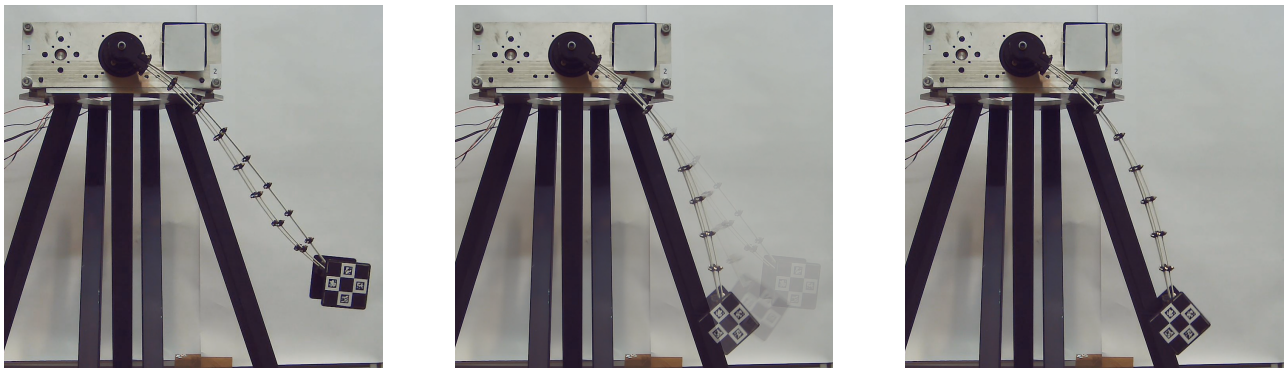

(a) (b) (c)

Figure 10: Snapping phenomenon at the $T2a$ curve: when quasi-statically reaching the singular configuration (a), the robot dynamically snaps (b), and it reaches a new stable configuration (c).

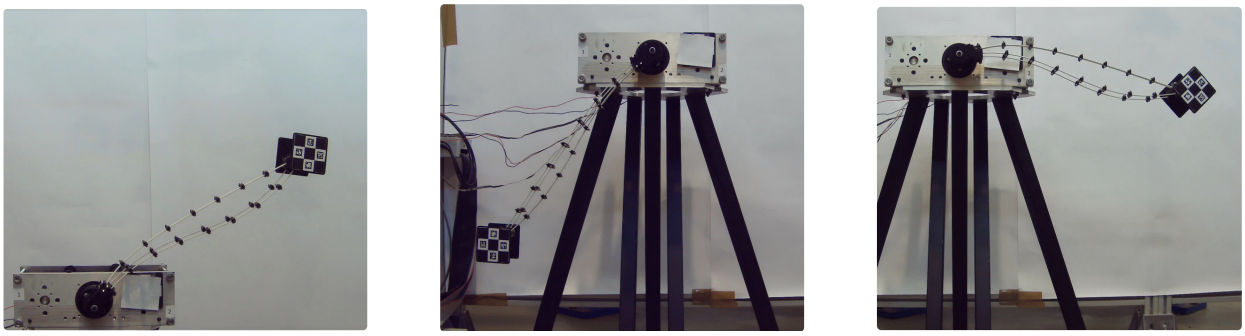

(a) (b) (c)

Figure 11: External border reconstruction. Three different configurations close to the singularity curve $T2a$ are illustrated.

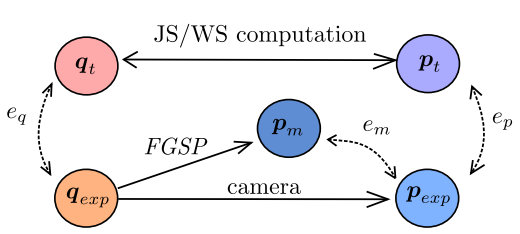


Figure 12: Graphical representation of the variables necessary for the errors definitions.

| | $e_q$ [°] | $e_p$ [mm] | $e_m$ [mm] |
|---|---|---|---|
| Mean | 2,68 | 23,13 | 19,37 |
| Median | 2,78 | 17,04 | 16,46 |
| Max | 6,56 | 67,53 | 45,50 |
| Dev.Std | 1,59 | 14,28 | 10,63 |

Table 1: Motor angles, *EE* position, and model errors for the $T2a$ reconstruction.

Fig. 12). We also define $e_m$ as:

$$e_m = \|\mathbf{p}_{exp} - \mathbf{p}_m\|_2 \tag{27}$$

where $e_m$ represents the model error. The mean value of $e_m$, obtained with the use of four assumed modes [34], is 18,56 mm (3,29 %), which is comparable to $e_p$. To exclude the discretization model by the causes of inacuraccy, we compared the $e_m$ obtained by the shooting-based model of [3],[49] and our model. By solving the *FGSP* over each $\mathbf{q}_{exp}$, the model of [3] results in a mean $e_m$ = 17,71mm, comparable to the results of our model.

### *5.3. Inner WS boundary*

The inner *WS* boundary if defined by singularity curve $TL$, where both $\mathbf{T}_1, \mathbf{T}_2$ are rank deficient since $\mathbf{U}$ is rank deficient. According to the terminology of [28], this is a leg singularity. This elastic equilibrium limit is different from the snapping phenomena of $T2a$. Similarly to $T2a$, a non-null *EE* motion occurs about the singularity curve even if the motors are braked. However, the uncontrolled *EE* motion results in an out-of-the-plane link deflection and *EE* motion (as illustrated in Fig. 13). A demo of this phenomenon is reported in the accompanying video at minute 0 second 38. When the robot lies in ①, the motors rotations generate only in-plane *EE* motion but, after crossing $TL$, the motors rotations generates an out-of-the-plane *EE* motion that was not possible before crossing $TL$ (even if this motion is not controllable).

We tested 22 different configurations with the *EE* uniformly placed on $TL$ (see Figs.14a, 14b, 14c for some near-singular configuration examples). As in the previous case, we focused on the motor error $e_q$, the *EE* position error $e_p$, and the model

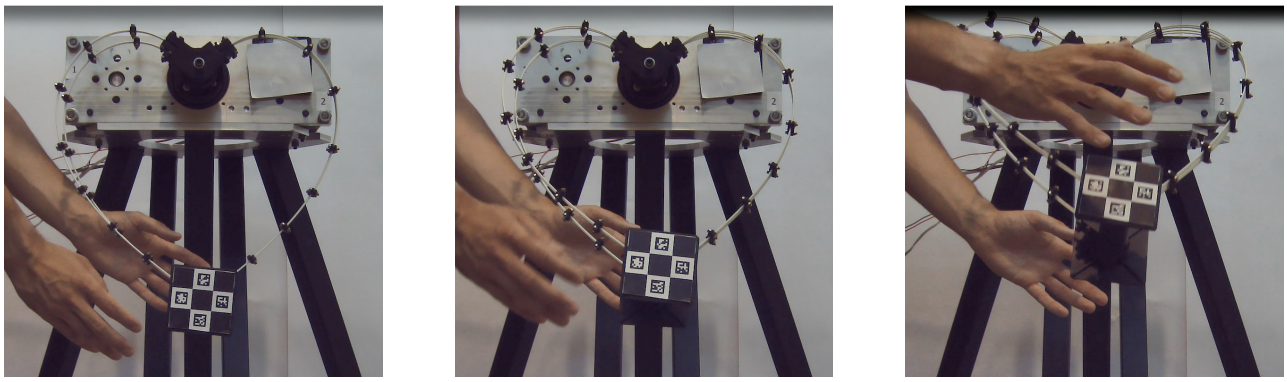

(a) (b) (c)

Figure 13: Instability at the $TL$ curve: when quasi-statically reaching the singular configuration (a), the robot *EE* moves out-of-the-plane (b). The *EE* is manually blocked (c) to not brake the robots legs.

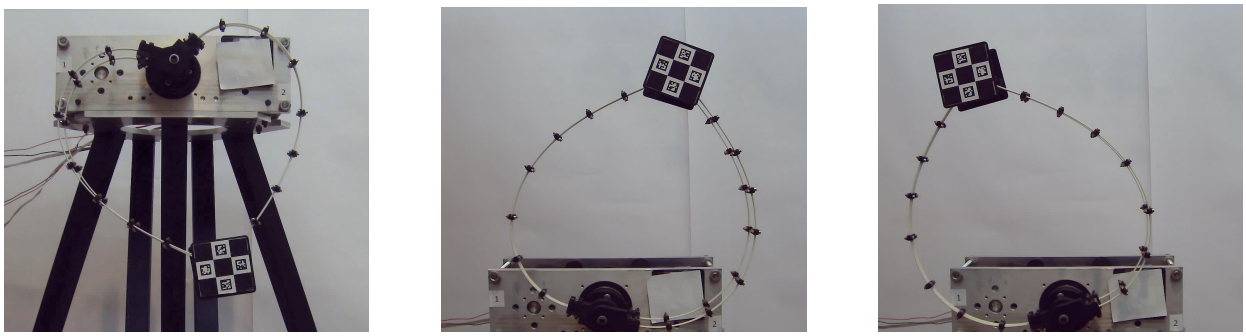

(a) (b) (c)

Figure 14: Inner border reconstruction. Three different configurations close to the singularity curve $TL$ are illustrated.

| | $e_q$ [°] | $e_p$ [mm] | $e_m$ [mm] |
|---|---|---|---|
| Mean | 4,17 | 27,86 | 20,59 |
| Median | 3,99 | 26,75 | 19,50 |
| Max | 8,03 | 44,77 | 31,52 |
| Dev.Std | 1,98 | 8,44 | 5,89 |

Table 2: Motor angles, *EE* position, and model errors for the $TL$ reconstruction.

error $e_m$ (Table 2 summarizes the results). We obtained a mean $e_q = 4.17°$, which corresponds to a mean $e_p = 27.86$ mm (4.94 % w.r.t. total link length of 564 mm).

As for $T2a$, we investigate the discretized-model error: the mean values of $e_m$, obtained with the use of four assumed modes [34], is 20,58 mm (3,65 %). A similar result is obtained with the shooting-based model of [3], with a mean error of $e_m = 19.11$ mm (3,39 %).

### *5.4. Discussion of the results*

Globally, we obtained a significant agreement between the experimental data and the equilibrium stability prediction provided by a full spatial model, as qualitatively illustrated in Fig. 9. In particular, we can state that the $TL$ singularity curve is correctly predicted by a spatial model only: this is reasonable since a planar model disregards out-of-the-plane phenomena. Although planar *CPRs* are frequently analyzed with planar models ([29],[42],[22]), this paper clearly showed that planar models are insufficient in predicting stability limits, and thus *JS*/*WS* limits of such a prototype.

The experimental reconstruction of $T2a$ and $TL$ curves confirm the accuracy of our equilibrium-stability prediction approach since the difference between theoretical and experimental motor angles at singularities ($e_q$) is very low ($\leq 5°$). The *EE* position error $e_p$, less than $\leq 5\%$ of the length of the link, is acceptable considering the current state-of-the-art (see [45]). As causes of errors, model simplification is one of the possible reasons, but we primarily need to consider that all the measurements are conducted in the proximity of singular configurations, where any small error (e.g. belt elasticity, gearbox clearance) may be possibly reflected in significant variations of the configuration variables. We tested the model accuracy in several stable positions far from singularities (see Fig. 9, stable points), and the average model error with four assumed modes is $e_m = 12.81$ mm (2.27 %), significantly lower than 19.37 mm and 20.59 mm of configurations near $T2a$ and $TL$, respectively.

To the authors' knowledge, this is the first time a singularity of matrix $\mathbf{U}$ is discovered and experimentally verified for *CPRs* with actuation at their base. In tendon-driven *CPRs*, singularities of $\mathbf{U}$ were identified in [45]. In that case, degeneracies of $\mathbf{U}$ were associated with leg singularities where multiple tendons were slack. However, the physical phenomena we experience is different. To better understand what happens in our case, let us

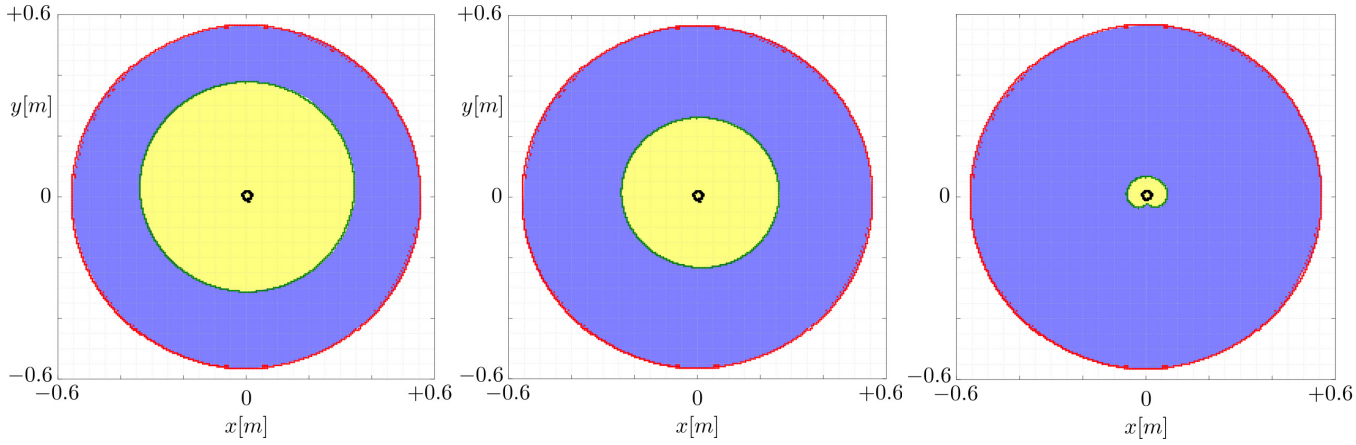


(a) $n_b = 8$ (b) $n_b = 20$ (c) $n_b = 50$

Figure 15: Comparison of *WS* by varying the number of connecting constraints ($n_b$). (a) the actual solution, $n_b = 8$, (b) $n_b = 20$, (c) $n_b = 50$. Stable and unstable configurations are depicted in blue and yellow, respectively. Type-1 singularities are shown in red, and Type-2 singularities in black. Singularities, where $\mathbf{U}$ is degenerate, are plotted in green.

consider the forward kinemato-static problem of Eq. (12), here reported:

$$\begin{bmatrix}\Delta\mathbf{q}_p\\ \Delta\mathbf{q}_d\end{bmatrix} = \mathbf{J}\Delta\mathbf{q}_a + \mathbf{C}\Delta\mathbf{f}_p \tag{28}$$

where $\mathbf{J} = -[\mathbf{P}\ \mathbf{U}]^{-1}\mathbf{A} \in \mathbb{R}^{(nc+m)\times m}$ is called Jacobian matrix, and $\mathbf{C} = -[\mathbf{P}\ \mathbf{U}]^{-1}\mathbf{W} \in \mathbb{R}^{(n_c+m)\times 3}$ is named compliance matrix. When the manipulator approaches the singularity curve $TL$, matrix $\mathbf{U}$ becomes rank deficient. Then, by inspection of $\mathbf{C}$, we noted that submatrix $\mathbf{C}_u$ relating $\Delta\mathbf{q}_u = \mathbf{C}_u\Delta\mathbf{f}_p$ is ill-conditioned, displaying negligible stiffness in the direction orthogonal to the robot motion plane. This further confirms the inability of the model with planar displacement assumptions in the identification of $TL$ since it fails to detect the lack of stiffness in the out-of-the-plane direction.

As the manipulator displays negligible stiffness in the direction orthogonal to the robot motion plane when approaching $TL$, we explore how the stiffness of the links influences this phenomenon. To do this, we vary the number of connecting constraints $n_b$, increasing the torsional stiffness of the beams (see Eq. (15)). Starting from the current solution with $n_b = 8$, by increasing the number of $n_b$, the unstable *WS* area reduces, as shown in Fig.15. In particular, by selecting $n_b \geq 50$, almost all the Cartesian *WS* is theoretically reachable.

## 6. Conclusions

This paper addressed the experimental validation of equilibrium stability of *CPRs* predictions. We demonstrated the inability of a model based on planar displacement assumptions to predict the equilibrium stability of a planar *CPR*. A new planar *CPR* was proposed for the scope. The prototype was designed to be nominally planar and such that no mechanical interference between robot components could occur. Because of the prototype architecture, we also originally proposed a material parameter modelling methodology for the specific design of the flexible chains employed. Finally, we experimentally identified

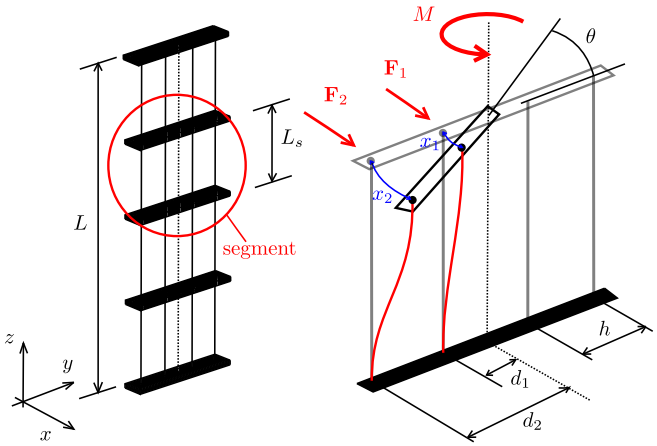


Figure 16: Derivation of distributed parameters

a singularity related to out-of-the-plane uncontrolled motions of the planar CPR for the first time.

## Appendix A. Distributed parameters derivation

As shown in Fig. 16, we model our flexible chain as a series of flexible segments, with $s = 1, \cdots, n_b$ indicating the index of each segment, and $n_b$ the number of segments. Segments are assumed to have the same length $L_s = L/n_b$ and, since we employ circular cross-section beams, $I_x = I_y = I$. We start by considering the inner chain made by four links: assuming the width of the intermediate constraints on the $z$ direction to be negligible, the flexible chain is equivalent to four beams in parallel, and $k_x$ is given by:

$$k_x = \sum_{i=1}^{4} k_{xi} = 4\frac{EI}{L^3}; \quad k_{xi} = \frac{EI}{L^3} \tag{A.1}$$

We then consider $k_y$: under small deformation assumptions[6], each segment is equivalent to four parallel beams clamped at both ends. Thus, the stiffness of each segment $k_{ys}$ can be simply obtained as:

$$k_{ys} = 4\frac{12EI}{L_s^3} = n_b^3\frac{48EI}{L^3} \tag{A.2}$$

and the overall stiffness $k_y$ is the stiffness of $n_b$ elements in series:

$$\frac{1}{k_y} = \sum_{s=1}^{n_b}\frac{1}{k_{ys}} \Rightarrow k_y = n_b^2\frac{48EI}{L^3} \tag{A.3}$$

The computation of the torsional stiffness is not as straightforward, and it is detailed below. First, let us consider Fig.16, where $h$ is the distance between the beams, assumed to be equal for each of them. Due to the symmetry of the system, we can obtain the $k_{zs}$ of $s$-th segment by considering only half system:

$$k_{zs} = 2k_b \tag{A.4}$$

where $k_b$ is the contribution of two beams. In order to characterize the torsional stiffness, we want to relate the torsion angle $\theta$ to the external moment $M$. An external moment $M$ is equivalent to two forces $F_1, F_2$ applied to the beams, that is:

$$M = F_1 d_1 + F_2 d_2 \tag{A.5}$$

where $d_1, d_2$ are the beams distances to the link centerline (see Fig.16). Then, by the application of $F_1$ and $F_2$, the beams display tip displacements $x_1$ and, $x_2$ respectively. By considering beams as clamped at both ends, assuming small deformations and the local beam torsion over its own axis to be negligible, $F_1, F_2$ are proportional to the tip displacements $x_1, x_2$ as follows:

$$F_1 = \frac{12EI}{L_s^3}x_1; F_2 = \frac{12EI}{L_s^3}x_2 \tag{A.6}$$

By inserting Eq. (A.6) into Eq. (A.5), we obtain:

$$M = \frac{12EI}{L_s^3}(x_1 d_1 + x_2 d_2) \tag{A.7}$$

Under small deformation assumptions, we can approximate $x_1 \simeq d_1\theta, x_2 \simeq d_2\theta$. Then, by introducing $d_1 = h/2, d_2 = 3h/2$, we obtain:

$$M = \frac{30EI}{L_s^3}h^2\theta \tag{A.8}$$

and we obtain $k_b$ by the definition of the torsional stiffness:

$$k_b = \frac{M}{\theta} = \frac{30EI}{L_s^3}h^2 \tag{A.9}$$

by inserting Eq. (A.9) into Eq. (A.4), we obtain:

$$k_{zs} = \frac{60EI}{L_s^3}h^2 = n_b^3\frac{60EI}{L^3}h^2 \tag{A.10}$$

Then, $k_z$ is the stiffness of $n_b$ torsional springs in series, that is:

$$\frac{1}{k_z} = \sum_{s=1}^{n_b}\frac{1}{k_{zs}} \Rightarrow k_z = 60n_b^2h^2\frac{EI}{L^3} \tag{A.11}$$

Finally, $\mathbf{K}_{BT}$ is obtained by normalizing over $L^3$:

$$\mathbf{K}_{BT-in} = EI\ \mathrm{diag}(4, 48n_b^2, 60n_b^2h^2) \tag{A.12}$$

where the subscript $()_{in}$ individuates the inner chain with four beams, and diag the 3×3 diagonal matrix whose entries are placed over its principal diagonal. Similarly, the stiffness of a single outer chain $\mathbf{K}_{BT-out}$ is:

$$\mathbf{K}_{BT-out} = EI\ \mathrm{diag}(2, 24n_b^2, 12n_b^2h^2) \tag{A.13}$$

[6]Please note that small deformations do not implicates small displacements.

## References


[1] J. Burgner-Kahrs, D. C. Rucker, H. Choset, Continuum robots for medical applications: A survey, IEEE Transactions on Robotics 31 (6) (2015) 1261–1280.

[2] C. E. Bryson, D. C. Rucker, Toward parallel continuum manipulators, in: 2014 IEEE International Conference on Robotics and Automation (ICRA), IEEE, 2014, pp. 778–785.

[3] C. B. Black, J. Till, D. C. Rucker, Parallel continuum robots: Modeling, analysis, and actuation-based force sensing, IEEE Transactions on Robotics 34 (1) (2017) 29–47.

[4] A. L. Orekhov, C. E. Bryson, J. Till, S. Chung, D. C. Rucker, A surgical parallel continuum manipulator with a cable-driven grasper, in: 2015 37th Annual International Conference of the IEEE Engineering in Medicine and Biology Society (EMBC), IEEE, 2015, pp. 5264–5267.

[5] A. L. Orekhov, V. A. Aloi, D. C. Rucker, Modeling parallel continuum robots with general intermediate constraints, in: 2017 IEEE International Conference on Robotics and Automation (ICRA), IEEE, 2017, pp. 6142–6149.

[6] O. Altuzarra, D. Caballero, F. J. Campa, C. Pinto, Forward and inverse kinematics in 2-DOF planar parallel continuum manipulators, in: Corves, B., Wenger, P., Hüsing, M. (eds) EuCoMeS 2018, Vol. 59, Springer, 2018, pp. 231–238.

[7] O. F. Gallardo, B. Mauze, R. Dahmouche, C. Duriez, G. J. Laurent, Turning an articulated 3-ppsr manipulator into a parallel continuum robot, in: 2021 IEEE/RSJ International Conference on Intelligent Robots and Systems (IROS), IEEE, 2021, pp. 4955–4960.

[8] G. Böttcher, S. Lilge, J. Burgner-Kahrs, Design of a reconfigurable parallel continuum robot with tendon-actuated kinematic chains, IEEE Robotics and Automation Letters 6 (2) (2021) 1272–1279.

[9] F. Campa, M. Diez, D. Diaz-Caneja, O. Altuzarra, A 2 *DoF* continuum parallel robot for pick & place collaborative tasks, in: Uhl, T. (eds) Advances in Mechanism and Machine Science. IFToMM WC 2019, Vol. 73, Springer, 2019, pp. 1979–1988.

[10] B. Mauze, G. J. Laurent, R. Dahmouche, C. Clevy, Micrometer positioning accuracy with a planar parallel continuum robot, Frontiers in Robotics and AI 8 (2021) 196.

[11] C. Armanini, F. Boyer, A. T. Mathew, C. Duriez, F. Renda, Soft robots modeling: A structured overview, IEEE Transactions on Robotics (2023).

[12] A. Chawla, C. Frazelle, I. Walker, A comparison of constant curvature forward kinematics for multisection continuum manipulators, in: 2018 Second IEEE International Conference on Robotic Computing (IRC), IEEE, 2018, pp. 217–223.

[13] S. Sadati, S. E. Naghibi, A. Shiva, I. D. Walker, K. Althoefer, T. Nanayakkara, Mechanics of continuum manipulators, a comparative study of five methods with experiments, in: Gao, Y., Fallah, S., Jin, Y., Lekakou, C. (eds) Towards Autonomous Robotic Systems. TAROS 2017. Lecture Notes in Computer Science(), Vol. 10454, Springer, 2017, pp. 686–702.

[14] M. T. Chikhaoui, S. Lilge, S. Kleinschmidt, J. Burgner-Kahrs, Comparison of modeling approaches for a tendon actuated continuum robot with three extensible segments, IEEE Robotics and Automation Letters 4 (2) (2019) 989–996.

[15] J. Jung, R. S. Penning, M. R. Zinn, A modeling approach for robotic catheters: effects of nonlinear internal device friction, Advanced Robotics 28 (8) (2014) 557–572.

[16] I. S. Godage, R. Wirz, I. D. Walker, R. J. Webster III, Accurate and efficient dynamics for variable-length continuum arms: A center of gravity approach, Soft Robotics 2 (3) (2015) 96–106.

[17] F. Renda, V. Cacucciolo, J. Dias, L. Seneviratne, Discrete cosserat approach for soft robot dynamics: A new piece-wise constant strain model with torsion and shears, in: 2016 IEEE/RSJ International Conference on Intelligent Robots and Systems (IROS), IEEE, 2016, pp. 5495–5502.

[18] D. C. Rucker, B. A. Jones, R. J. Webster III, A geometrically exact model for externally loaded concentric-tube continuum robots, IEEE transactions on robotics 26 (5) (2010) 769–780.

[19] A. Jalali, F. Janabi-Sharifi, Dynamic modeling of tendon-driven comanipulative continuum robots, IEEE Robotics and Automation Letters 7 (2) (2021) 1643–1650.

[20] A. L. Orekhov, C. B. Black, J. Till, S. Chung, D. C. Rucker, Analysis and validation of a teleoperated surgical parallel continuum manipulator, IEEE Robotics and Automation Letters 1 (2) (2016) 828–835.

[21] G. Wu, G. Shi, Experimental statics calibration of a multi-constraint parallel continuum robot, Mechanism and Machine Theory 136 (2019) 72–85.

[22] K. Nuelle, T. Sterneck, S. Lilge, D. Xiong, J. Burgner-Kahrs, T. Ortmaier, Modeling, calibration, and evaluation of a tendon-actuated planar parallel continuum robot, IEEE Robotics and Automation Letters 5 (4) (2020) 5811–5818.

[23] G. Chen, Y. Kang, Z. Liang, Z. Zhang, H. Wang, Kinetostatics modeling and analysis of parallel continuum manipulators, Mechanism and Machine Theory 163 (2021) 104380.

[24] X. Duan, W. Yan, G. Chen, H. Wang, Analysis and validation of a planar parallel continuum manipulator with variable cartesian stiffness, Mechanism and Machine Theory 177 (2022) 105030.

[25] H. Pan, G. Chen, Y. Kang, H. Wang, Design and kinematic analysis of a flexible-link parallel mechanism with a spatially quasi-translational end effector, Journal of Mechanisms and Robotics 13 (1) (2021).

[26] J. Till, D. C. Rucker, Elastic stability of cosserat rods and parallel continuum robots, IEEE Transactions on Robotics 33 (3) (2017) 718–733.

[27] H. B. Gilbert, R. J. Hendrick, R. J. Webster III, Elastic stability of concentric tube robots: A stability measure and design test, IEEE Transactions on Robotics 32 (1) (2015) 20–35.

[28] S. Briot, A. Goldsztejn, Singularity conditions for continuum parallel robots, IEEE Transactions on Robotics 38 (1) (2021) 507–525.

[29] O. Altuzarra, D. Caballero, F. J. Campa, C. Pinto, Position analysis in planar parallel continuum mechanisms, Mechanism and Machine Theory 132 (2019) 13–29.

[30] F. Zaccaria, E. Idá, S. Briot, M. Carricato, Workspace computation of planar continuum parallel robots, IEEE Robotics and Automation Letters 7 (2) (2022) 2700–2707.

[31] J.-P. Merlet, D. Daney, Legs interference checking of parallel robots over a given workspace or trajectory, in: Proceedings 2006 IEEE International Conference on Robotics and Automation, 2006. ICRA 2006., IEEE, 2006, pp. 757–762.

[32] L. Campos, F. Bourbonnais, I. A. Bonev, P. Bigras, Development of a five-bar parallel robot with large workspace, in: International Design Engineering Technical Conferences and Computers and Information in Engineering Conference, Vol. 44106, 2010, pp. 917–922.

[33] F. Zaccaria, E. Idá, S. Briot, A Boundary Computation Algorithm for the Workspace Evaluation of Continuum Parallel Robots, Journal of Mechanisms and Robotics 16 (4) (2023).

[34] S. Briot, F. Boyer, A geometrically exact assumed strain modes approach for the geometrico-and kinemato-static modelings of continuum parallel robots, IEEE Transactions on Robotics (2022).

[35] B. Mauzé, R. Dahmouche, G. J. Laurent, A. N. André, P. Rougeot, P. Sandoz, C. Clévy, Nanometer precision with a planar parallel continuum robot, IEEE Robotics and Automation Letters 5 (3) (2020) 3806–3813.

[36] S. Antman, Nonlinear Problems of Elasticity, Vol. 107, Springer Verlag New York, 1995.

[37] F. Boyer, V. Lebastard, F. Candelier, F. Renda, Dynamics of continuum and soft robots: A strain parameterization based approach, IEEE Transactions on Robotics 37 (3) (2020) 847–863.

[38] J. Nocedal, S. Wright, Numerical Optimization, 2nd Edition, Springer, 2006.

[39] S. Briot, F. Boyer, Technical report associated with the paper: A geometrically-exact assumed strain modes approach for the geometricoand kinemato-static modellings of continuum parallel robots, Tech. Rep. 03836288, Laboratoire des Sciences du Numérique de Nantes (LS2N) (2022).
URL `https://hal.archives-ouvertes.fr/hal-03836288`

[40] R. J. Webster III, B. A. Jones, Design and kinematic modeling of constant curvature continuum robots: A review, The International Journal of Robotics Research 29 (13) (2010) 1661–1683.

[41] F. Renda, F. Boyer, J. Dias, L. Seneviratne, Discrete cosserat approach for multisection soft manipulator dynamics, IEEE Transactions on Robotics 34 (6) (2018) 1518–1533.

[42] F. Zaccaria, S. Briot, M. T. Chikhaoui, E. Idá, M. Carricato, An analytical formulation for the geometrico-static problem of continuum planar parallel robots, in: Venture, G., Solis, J., Takeda, Y., Konno, A. (eds) ROMANSY 23 - Robot Design, Dynamics and Control. ROMANSY 2020. CISM International Centre for Mechanical Sciences, Vol. 601, Springer, 2020, pp. 512–520.

[43] B. S. Institution, BS EN 13706–2:2002: Reinforced Plastic Composites - Specification for Pultruded Profiles - Part 2: Methods of Test and General Requirements, BSI Standards Limited, London, United Kingdom, 2002.

[44] B. A. Jones, R. L. Gray, K. Turlapati, Three dimensional statics for continuum robotics, in: 2009 IEEE/RSJ International Conference on Intelligent Robots and Systems, IEEE, 2009, pp. 2659–2664.

[45] S. Lilge, J. Burgner-Kahrs, Kinetostatic modeling of tendon-driven parallel continuum robots, IEEE Transactions on Robotics (2022) 1–17`doi:10.1109/TRO.2022.3226157`.

[46] S. M. Kay, Fundamentals of statistical signal processing: estimation theory, Prentice-Hall, Inc., 1993.

[47] G. Bradski, The opencv library., Dr. Dobb's Journal: Software Tools for the Professional Programmer 25 (11) (2000) 120–123.

[48] D. Zlatanov, I. A. Bonev, C. M. Gosselin, Constraint singularities of parallel mechanisms, in: Proceedings 2002 IEEE International Conference on Robotics and Automation (Cat. No. 02CH37292), Vol. 1, IEEE, 2002, pp. 496–502.

[49] A. Gotelli, F. Zaccaria, O. Kermorgant, S. Briot, A gazebo simulator for continuum parallel robots, in: Altuzarra, O., Kecskeméthy, A. (eds) Advances in Robot Kinematics 2022. ARK 2022. Springer Proceedings in Advanced Robotics, Vol. 24, Springer, 2022, pp. 248–256.